**Atmospheric
Chemistry
and Physics
Discussions**

Feedback between dust particles and atmospheric processes over West Africa in March 2006 and June 2007

T. Stanelle[1,*], B. Vogel[1], H. Vogel[1], D. Bäumer[1,], and Ch. Kottmeier[1]**

[1]Institute for Meteorology and Climate Research, Karlsruhe Institute of Technology, Germany
[*]now at: Institute for Atmospheric and Climate Science, Swiss Federal Institute of Technology (ETH), Zurich, Switzerland
[**]now at: BASF, Ludwigshafen, Germany

Correspondence to: B. Vogel (bernhard.vogel@kit.edu)

ACPD

10, 7553–7599, 2010

Feedback between dust particles and atmospheric processes

T. Stanelle et al.

Title Page

Abstract	Introduction
Conclusions	References
Tables	Figures

|◄|►|

|◄|►|

| Back | Close |

Full Screen / Esc

Printer-friendly Version

Interactive Discussion

Abstract

We used the comprehensive model system COSMO-ART to quantify the impact of mineral dust on the radiative fluxes, the temperature and the feedback between dust particles and their emissions. We simulated two dust storms over West Africa in March 2006 and in June 2007. Simulations with and without coupling of the actual dust concentration with the radiative fluxes and the thermodynamics were carried out for each case. The model results for the 2006 case were compared with observations of the AMMA campaign.

At the surface the shortwave radiative effect of mineral dust can be described by a linear relation between the changes in net surface radiation and the aerosol optical depth. For an aerosol optical depth (AOD) at 450 nm of 1 the average shortwave radiation reduction amounts $-130 \, \mathrm{W \, m^{-2}}$ during noon. The longwave radiative effect of mineral dust is nonlinear, with an average increase of $+70 \, \mathrm{W \, m^{-2}}$ for an AOD (450 nm) of 1. At the top of the atmosphere the effect of the dust layer with an AOD of 1 on radiative fluxes is not as significant as at the surface. It is slightly positive for the shortwave and approximately $26 \, \mathrm{W \, m^{-2}}$ for the longwave radiation.

The height range and the extension of the dust layer determine the effect of dust particles on the 2 m temperature. When the dust layer is attached to the surface and lasts for several days it leads to an increase of the surface temperature even during daytime. In case of an elevated dust layer there is a decrease in 2 m temperature of up to 4 K during noon.

It is shown, that the temperature changes caused by mineral dust may result in horizontal temperature gradients which also modify near surface winds. Since surface wind thresholds decide the uptake of dust from the surface, a feedback on total emission fluxes is established. The coupled model provides an increase in the total emission fluxes of dust particles by about 16% during the dust storm in March 2006 and 25% during the dust episode in June 2007.

1 Introduction

Mineral dust and sea salt are the most important sources of aerosol mass for the atmosphere (Seinfeld and Pandis, 1998). Dust is involved in many important processes in Earth's climate system. These processes include nutrient transport into the ecosystem (Martin, 1990; Swap et al., 1992; Prospero, 1999), the direct radiative forcing (e.g., Tegen et al., 1996), and the indirect radiative effect (e.g., Hoose et al., 2008). Desertification due to human activities or caused by climate change also will have an impact on the emissions of mineral dust particles (Nicholson et al., 1998) and vice versa. Mineral dust particles affect the atmospheric radiation budget directly by absorption and scattering of incoming solar radiation, and absorption and re-emission of outgoing longwave radiation. Mineral dust particles have an impact on cloud formation and therefore on the indirect aerosol effect as well (IPCC, 2007). Mineral dust particles may increase the number of cloud-condensation (CCN) and ice nuclei. In case of CCN the increase leads to enhanced cloud albedo and to prolonged lifetimes of clouds. While the scattering of solar radiation and the indirect aerosol effect tend to cool the atmosphere, the absorption of radiation by aerosols leads to a warming of atmosphere and to a suppression of cloud formation (semi-direct effect) (e.g., Twomey et al., 1984; Albrecht, 1989; Charlson et al., 1992; Schwartz, 1996; Rosenfeld, 2000; Ackermann et al., 2000; Chameides et al., 2002; Nenes et al., 2002; Cook and Highwood, 2004; Johnson et al., 2004; Helmert et al., 2007). Estimates of the global radiative forcing of mineral dust vary between $-0.56\,\mathrm{W\,m^{-2}}$ and $+0.1\,\mathrm{W\,m^{-2}}$ (IPCC, 2007) which shows its relatively large cooling effect but also the high uncertainty.

The uncertainty is largely determined by insufficiently quantified processes. Many studies have investigated the direct radiative forcing of mineral dust particles on the global scale (e.g., Tegen et al., 1996; Miller et al., 2004; Perlwitz et al., 2001; Yoshioka et al., 2007). But these studies were done with a coarse spatial resolution of soil data and meteorological fields. This creates large uncertainties (Zender et al., 2003).

For numerical weather prediction models Kischa et al. (2003) and Haywood et

al. (2005) suggest that a correct treatment of mineral dust and its radiative effects would improve the representation of the radiation budget and the accuracy of the weather prediction itself. Recently, regional dust transport models have been developed and coupled to numerical weather prediction models (e.g., Nickovic et al., 2001; Tegen et al., 2006; Heinold et al., 2007; Tulet et al., 2008). For modelling the influence of dust particles on the radiation budget, the emission and transport of dust particles must be calculated. In addition the refractive indices of the dust particles have to be known. Its real and imaginary parts represent the reflective and absorptive properties, respectively. The refractive indices depend considerably on the mineralogical composition. The mineralogical composition of dust particles has a strong dependence on the source region (Formenti et al., 2008; Petzold et al., 2009).

Helmert et al. (2007) investigated the sensitivity of radiative forcing and its impact on atmospheric dynamics and dust optical properties with the regional dust model LM-MUSCAT-DES. They show that the large variability in radiative properties due to different mixtures of clay aggregates found in Saharan dust can lead to high differences in the radiation budget. For a quantification of the effects of mineral dust on the radiation budget they used the mean radiative efficiency. The radiative efficiency is the radiative forcing produced by an aerosol optical depth (AOD) of 1 and is a function of height. They found a mean shortwave radiative efficiency of $-196\,\mathrm{W\,m^{-2}}$ for prevailingly reflecting dust particles and $-220\,\mathrm{W\,m^{-2}}$ for prevailingly absorbing dust particles at the surface in the southern Sahara. The longwave radiative efficiency was determined to be about $60\,\mathrm{W\,m^{-2}}$ and $64\,\mathrm{W\,m^{-2}}$, respectively for the prevailingly absorbing dust particles. Milton et al. (2008) found a reduction in net downward shortwave flux at the surface with a maximum of $-200\,\mathrm{W\,m^{-2}}$ for a dust storm that occurred over West Africa in March 2006.

Tulet et al. (2008) and Mallet et al. (2009) used the standard formulation of absorption and reemission of longwave radiation for aerosols from the ECMWF model in the MESO-NH model. They added a fraction of the 550 nm optical depth to the longwave optical depth of CO_2 and H_2O. This fraction is constant for each aerosol type (ECMWF,

2004). This assumption results in inaccuracies in the calculations of the longwave radiative effect, however (Grini et al., 2006). Changes in the radiative fluxes have an influence on surface and air temperature. Mallet et al. (2009) found a reduction of surface temperature of up to 4 K over regions where high aerosol optical depths (AOD)

5 occur. For the initial stage of a dust storm in March 2005, Tegen et al. (2006) found a decrease in maximum daytime temperatures of about 5 K. Helmert et al. (2007) detected a decrease of 3 K for more reflecting particles and 3.3 K for more absorbing ones as a regional average for the southern Sahara.

In our study we will analyse the observations and model results of two dust episodes

10 that occurred over West Africa. We performed our model runs with the regional model system COSMO-ART (COSMO: COnsortium for Small-scale MOdelling, Steppeler et al., 2002; ART: Aerosols and Reactive Trace gases, Vogel et al., 2009). In contrast to the studies of Tulet et al. (2008) and Mallet et al. (2009) we consider the optical properties of the whole spectral range.

15 We simulated the influence of mineral dust particles on the state of the atmosphere for two dust episodes. The first episode is a dust outbreak that occurred during the African Multidisciplinary Monsoon Analysis (AMMA, Redelsperger et al., 2006) campaign in March 2006. The second episode occurred during June 2007 when the GERBILS (Geostationary Earth Radiation Budget experiment Intercomparison of Longwave

20 and Shortwave radiation) field campaign took place in West Africa (Marsham et al., 2008).

The COSMO-ART model and the performed model runs are described in brief, and we give a short overview of the evolution of the dust storm in March 2006. We compare our model results with the available measurements. Especially, a detailed comparison

25 of modelled and observed radiative fluxes is shown for Niamey.

We carried out two different model runs for each episode: The first one considers the feedback between mineral dust particles and radiative fluxes; the second one neglects it. On the basis of these runs we analyse the influence of dust particles on the radiative fluxes. We neglect the interaction of the mineral dust particles with cloud microphysics.

Feedback between dust particles and atmospheric processes

T. Stanelle et al.

Changes in near surface temperature caused by mineral dust are analysed for the episode in March where dust particles were located in the boundary layer and for the dust episode in June 2007 where also an elevated dust layer was found. Finally, we quantify the impact of the induced changes of the radiative fluxes on the emissions of
5 dust particles.

2 The COSMO-ART model system

COSMO-ART (Vogel et al., 2009) describes the emission, the transport, and the deposition of gases and aerosols and their feedback with the physical state variables of the atmosphere. The model system is fully online coupled and identical numerical methods
10 are applied to calculate the transport of all scalars. This also includes the treatment of deep convection with the Tiedtke scheme (Tiedtke, 1989), whereas the interaction of the mineral dust particles with cloud microphysics is not considered. Mineral dust particles are represented by log-normal distributions. Emission of dust particles are online calculated as functions of friction velocity, soil moisture, and surface parameters
15 (Vogel et al., 2006).

2.1 The dust emission scheme

The dust emission scheme used in COSMO-ART developed by Vogel et al. (2006) combines a parameterisation of the threshold friction velocity after Lu and Shao (1999) with a parameterisation of the saltation process after Alfaro and Gomes (2001). The
20 dust emission flux depends mainly on the friction velocity u_*. Dust emission takes place if u_* is larger than the threshold friction velocity, which depends on soil water content and surface roughness. These dependences are parameterised after Fécan et al. (1999) and Alfaro and Gomes (1995). Other key parameters for the calculation of the dust emissions are the soil properties. We are using soil properties (Table 1) that were
25 published by Marticorena et al. (1997) and Callot et al. (2000). The data set includes

7558

a classification of 13 different sand types. Each soil type contains information of up to three size distributions of particles including the median diameter and the standard deviation.

The calculation of the emission fluxes requires several input parameters for each surface grid box. Friction velocity and soil moisture are calculated within COSMO-ART at each time step. The fraction of erodible surface and the surface roughness are taken from the dataset of Chatenet et al. (1996). The residual soil moisture content, which is required for the calculation of the threshold friction velocity, is taken from Fécan et al. (1999).

COSMO-ART describes the size distribution of the mineral dust particles by three individual modes. The size distributions of each mode are approximated by a lognormal distribution with initial median diameters and standard deviations listed in Table 2. The emission scheme is coupled online with the COSMO-ART model.

At each grid point up to five different soil types are taken into account. The vertical dust flux ($F_{tv,i,s}$) is calculated for each soil type s separately. The individual fluxes are summed up weighted by the fraction $a(s)$ of the soil type s of each grid box:

$$F_{tv,i,\text{ges}} = \sum_{s=1}^{5} F_{tv,i,s} \cdot a(s)$$

This emission flux serves as the lower boundary condition for COSMO-ART.

2.2 The radiation scheme

The radiation scheme GRAALS that used in the COSMO model is based on the parameterisations of Ritter and Geleyn (1992). The transfer of shortwave and longwave radiation is calculated separately for non-cloudy and cloudy conditions. The scheme is based on the solution of the δ-two-stream version of the radiative transfer equation. Effects of scattering, absorption and emission by aerosol particles, gases and cloud droplets are taken into account. The solar spectrum is divided into three spectral

bands, which cover the wavelength interval between 0.25 µm and 4.64 µm. The terrestrial spectrum covers the wavelength interval between 4.64 µm and 104.5 µm. It is divided into five different spectral bands. Rayleigh scattering of molecules is considered for the shortwave spectral bands.

Scattering and absorption by aerosols on the radiative transfer are considered in all spectral intervals. Therefore, the radiation scheme follows an approach of Tanre et al. (1984). For solving the radiative transfer equation the knowledge of the optical thickness for absorption and scattering and of the asymmetry parameter of the aerosol types is required for each spectral band.

In the operational COSMO model aerosol particles are not explicitly treated. Moreover their effect on atmospheric radiation is accounted for by prescribed optical properties with an exponential decrease with height. All aerosol optical properties are fixed in time. The aerosol types are classified as "urban", "continental", and "maritime" for the troposphere and "volcanic" and 'stratospheric background aerosol" for the stratosphere. "Desert dust" aerosol is part of the "continental" aerosol type. "Rural" and "background tropospheric" aerosol are also assigned to this type of aerosol. The radiation scheme takes into account optical properties of these aerosol types for the eight spectral intervals.

"Desert dust" aerosol dominates the "continental" aerosol over Africa in the standard COSMO model (Helmert et al., 2007). Over the central Sahara the optical thickness at 550 nm wavelength for 'desert dust' aerosol alone is greater than 0.6. It is decreasing towards higher latitudes.

In order to quantify the effect of the online calculated aerosol distribution of desert aerosol on the radiative fluxes and thereby on the state of the atmosphere we carried out control runs (CTRL) without the prescribed optical properties of desert dust aerosol.

2.3 Online calculation of the optical properties within COSMO-ART

During intensive mineral dust events the dust optical thickness can reach values greater than three over Africa and the distribution of dust particles has a high variability in time

Feedback between dust particles and atmospheric processes

T. Stanelle et al.

and space. Therefore, the fixed optical properties of the aerosol class "desert dust" that are prescribed in the operational COSMO model are replaced by the online calculated ones. The aerosol optical thickness for scattering and absorption is calculated from the extinction coefficient b and the single scattering albedo ϖ. These parameters and the asymmetry factor g depend on particle size, number density and the complex refractive index of the particles. They are parameterised applying Mie theory. Particle size and number density distributions are calculated online with COSMO-ART.

The refractive index which is a crucial parameter for the Mie calculations depends on the wavelength of the radiation and the mineralogical composition of the dust parti-cles. In reality the mineralogical composition and therefore the refractive indices differ for dust particles originating from different source regions. This is shown by several measurements (e.g. Petzold et al., 2009; Formenti et al., 2008). For our model runs we assume that the mineralogical composition of the dust particles does not vary in time and space. We used the shortwave refractive indices that were measured during the SAMUM (SAharan Mineral dUst experiMent) campaign (Petzold et al., 2009; red line in Fig. 1). In the longwave spectral range we used refractive indices provided by Tegen (personal communication; blue line in Fig. 1). They are derived with the assumption of a mineralogical composition of 98% Kaolinite and 2% Hematite (Helmert et al., 2007). An overview of different measured values of refractive indices for mineral dust particles is given in Fig. 1.

When calculating the optical properties we assume that dust particles are spherical. This assumption results in negligible errors when using a 2-stream approximation as GRAALS (Mishchenko, personal communication). Mallet et al. (2009) performed opti-cal calculations using mixtures of oblate and prolate spheroids. They concluded that differences in the single scattering albedo and the asymmetry factor between these and spherical particles are lower than 10%. With this assumption it is possible to de-rive the optical properties by applying Mie theory. The Mie code we use in our study is based on an algorithm provided by Bohren and Huffman (1983). The calculation of the optical properties at each grid point and at each time step is very time consuming. For

Feedback between dust particles and atmospheric processes

T. Stanelle et al.

that reason we calculate the specific extinction coefficient, the single scattering albedo and the asymmetry parameter a priori for the three initial dust size distributions. The median diameters and the standard deviation of those distributions are given in Table 2. The derived values for the specific extinction coefficient, single scattering albedo and asymmetry factor for the three dust modes for each wavelength are then interpolated and weighted with the solar radiance for determining the values for the 8 spectral bands. The results are presented in Table 3. These values are input parameters for COSMO-ART.

Finally, the scattering and absorption optical thickness ($\tau_{s,k}$, $\tau_{a,k}$), and the asymmetry factor (g_k) are calculated from the specific extinction coefficient ($\tilde{b}_{e,n,k}$), the single scattering albedo ($\tilde{\omega}_{n,k}$), and the asymmetry factor ($\tilde{g}_{n,k}$) for each mode n and spectral band k:

$$b_{e,k}(x,y,z) = \sum_{n=1}^{3} \tilde{b}_{e,n,k} \cdot M_n(x,y,z) \tag{1}$$

$$\omega_k(x,y,z) = \frac{1}{b_{e,k}(x,y,z)} \cdot \sum_{n=1}^{3} \tilde{\omega}_{n,k} \cdot \tilde{b}_{e,n,k} \cdot M_n(x,y,z) \tag{2}$$

$$b_{s,n,k} = \tilde{\omega}_{n,k} \cdot \tilde{b}_{e,n,k} \cdot M_n(x,y,z) \tag{3}$$

$$g_k(x,y,z) = \frac{1}{\sum_{n=1}^{3} b_{s,n,k}} \cdot \sum_{n=1}^{3} \tilde{g}_{n,k} \cdot b_{s,n,k} \tag{4}$$

$$\tau_k(x,y,z) = b_{e,k}(x,y,z) \cdot (h(x,y,z) - h(x,y,z-1)) \tag{5}$$

$$\tau_{s,k}(x,y,z) = \omega_k(x,y,z) \cdot \tau_r(x,y,z) \tag{6}$$

$$\tau_{a,k}(x,y,z) = \tau_k(x,y,z) - \tau_{s,k}(x,y,z) \tag{7}$$

The index n refers to the three individual modes of mineral dust particles in COSMO-ART. $h(x,y,z)$ is the altitude of the model layer z above the ground, M_n is the actual mass concentration of mineral dust of the mode n.

The calculations according to Eqs. (1–7) are carried out online within COSMO-ART. As the radiative fluxes are modified by the mineral dust particles changes in the wind field and thermal stability occur. This induces modifications of the friction velocity. The friction velocity plays a key role in the calculation of the dust emission within COSMO-ART. Changes in dust emission and meteorological parameters induce changes in dust concentration and by that are closing the feedback loop.

3   Model setup

The simulation period for the synoptic induced dust storm is 5–10 March 2006. The period of the second dust storm is 19–24 June 2007. The simulation area for both episodes is West Africa (Fig. 2). The horizontal resolution for the model runs is 28 km. We used a time step of 45 s. Initial and boundary conditions are taken from the analyses of the IFS model of ECMWF (IFS: Integrated Forecast System; ECMWF: European Centre for Medium-Range Weather Forecasts). Initial and boundary conditions for mineral dust are set equal zero.

We replaced the surface albedo that is used in the standard COSMO model by data derived from MODIS data (Moderate Resolution Imaging Spectroradiometer; http://www-modis.bu.edu/brdf/userguide/albedo.html) as it is done by the IFS model. While the maximum values are below or equal 0.3 in the standard version of the COSMO model the MODIS product gives values of about 0.5 for desert areas.

The calculation of the horizontal saltation flux requires the knowledge of the emission constant C (Eq. 14; Vogel et al., 2006). This constant expresses the amount of material which is available for emission. This amount can vary during a dust event. White (1979) derived a value for C of 2.61 by theoretical considerations, whereas Gomes et al. (2003) found $C = 0.02$ during a field experiment in Spain. In our simulations we used

Feedback between dust particles and atmospheric processes

T. Stanelle et al.

|◄ | ►|

◄ | ►

Back | Close

Full Screen / Esc

$C = 0.8$.

Two different model runs were carried out for each dust episode. Run F includes the feedback between mineral dust particles and radiative fluxes. In run CTRL this feedback is neglected but the emission and transport of dust particles is considered. The radiation routine was called once per hour. With this configuration of model runs we determine the interaction of dust particles and the thermodynamic and dynamic processes over West Africa.

4 Comparison with observations

In March 2006 one of the biggest dust storms during the last years took place. It developed over Morocco and Algeria on 5 March 2006 when a cold front of a cyclone over the Balearic Islands reached Northern Africa. During the following days the cold front crossed West Africa accompanied by the dust storm. A description of the synoptic-dynamic evolution of the dust storm is included in Milton et al. (2008). They point out the similarity to a dust storm over West Africa in March 2004, which was analysed in detail by Knippertz et al. (2006).

4.1 Comparison with satellite data

During 5 March 2006, around noontime, major emissions of mineral dust particles occur over Algeria and Libya. A cold front moves to the south accompanied by the dust storm. During night time the emission flux of particles declines. Figure 3 shows the modelled aerosol optical depth (AOD, left) and the EUMETSAT RGB dust product (right) during 6–8 March 2006, 12:00 UTC respectively. The RGB dust product is derived from differences amongst three SEVIRI infrared channels (8.7 µm, 10.8 µm, and 12.0 µm). Dust appears in pink, high optically thick and cold clouds are coloured in dark red.

At noon of 6 March, significant dust emissions are simulated over West Africa (not

shown here) north of 16° N except in Morocco and north-west Algeria. The emitted dust particles are transported with high wind speeds in southerly directions. Algeria, Libya, and parts of Mauritania and Mali are under the influence of the dust storm on 6 March, 12:00 UTC (Fig. 3, top). The position of the simulated dust storm is in good
5   agreement with the observed one given by the dust product.

On 7 March 2006, 12:00 UTC, the observed dust front moves across the Hoggar, Air and Tibesti mountains. At that time the simulated emission fluxes reach their maximum. The flow is channelled by the topography and wind speed close to the surface increases. The intensification of the dust plume in these areas (Fig. 3, middle) is indi-
10 cated by the simulation as well. The small scale structure of the observed dust front cannot be resolved by the model results due to the horizontal resolution of 28 km. Nevertheless, the general position of the simulated dust storm is in good agreement with the observation.

Based on the relative vorticity which is a good indicator for the cold front we derived
15 the propagation of the dust front. On 6 March the position of the front is located around 28° N. Twenty-four hours later the front line is calculated to be around 10° further south. That means that the obtained mean velocity of the front was 13 m s^{-1}.

One day later (8 March) the dust storm has propagated further to the south. The simulated emission fluxes are now smaller than the day before. Again, the position
20 of the dust front is well reproduced by COSMO-ART. Small differences in the position and the structure especially in the south-east of the dust front are due to the coarse resolution.

4.2   Comparison with sun photometer data

A quantitative comparison of the dust evolution can be gained using AERONET sta-
25 tions (AErosol RObotic NETwork). In March 2006, the following AERONET stations located in our model domain performed measurements: Dakar, Agoufou, Maine Soroa, Cinzana, Tamanrasset, Banizoumbou, Djougou, Quagadougou, and Ilorin. We restrict to show the comparisons of observations and model results for the first four stations

(Fig. 4). The comparisons for the other stations give similar results. We compare the observed AOD at 440 nm with the simulated ones at 450 nm.

In general COSMO-ART captures the rise of the AOD during 7–9 March quite well. But the maxima in observed AOD are underestimated by the model. The temporal evo-
5 lution of the observed AOD is well reproduced by the modelled one for Dakar (Fig. 4). The comparison between modelled and observed AOD in Agoufou and Cinzana shows a delay in the simulated arrival of the dust front (Fig. 4). On 5 March the AOD is significantly underestimated for Maine Soroa by the model results. This is caused by the fact, that we start our simulations with a dust free atmosphere. Therefore the model
10 is not able to capture the observed values at the beginning of the simulation period. Our results are comparable to those of Tulet et al. (2008) for Ilorin and Djougou, and those of Milton et al. (2008) for Agoufou, Dakar, Cape Verde, Cinzana, Banizoumbou, Djougou, and Maine Soroa. The reason for the differences between model results and observed AOD could be both an imprecise calculated mass concentration and the un-
15 certainties of the refractive index and the size distributions that are used to calculate the optical properties. Another reason for the differences of modelled and measured AOD could be that the simulated AOD takes only dust particles into account whereas the measurements capture also other aerosol types. During the first three days (5–7 March) the measured Ångstrom coefficient (440 nm and 870 nm) is higher than 0.4.
20 This implies the presence of smaller particles like biomass burning aerosol. When the dust front reaches the station the value declines to less than 0.15, indicating the presence of larger particles. So the increase of observed AOD is due to the arrival of dust particles.

4.3   Comparison with data from SYNOP stations

25 We used the data of the SYNOP stations Hombori and Djanet (WMO No. 612400, 606700) for comparison. Djanet is located east of the Hoggar, Hombori is located further south (Fig. 2). Figure 5 shows time series of observed visibility and simulated AOD at 450 nm and observed and simulated 2 m temperature.

Printer-friendly Version

Interactive Discussion

CC BY

Observed visibility and simulated AOD are anti correlated at both stations. As the simulated dust is located in the boundary layer our model reproduces the arrival of the dust front and the further development at both stations very well.

The dust front arrives at Djanet during the night of 6–7 March 2006 and the observed
5 temperature decreases. The runs F and CTRL reproduce the decrease in temperature during the arrival of the dust front. This indicates that the decrease in temperature of about 10 K is caused by the passage of the cold front arriving simultaneously. After the arrival of mineral dust the 2 m temperature is better reproduced by run F than by run CTRL. The observed daily temperature range decreases from 14.1 K on 5 March
10 to 6.2 K on 7 March (Table 4). The simulated daily temperature range is reduced by 6.3 K in run F and by 4.1 K in run CTRL. A part of the reduction is due to the passage of the cold front but the presence of the dust particles causes a further reduction of the daily temperature range. The high dust concentrations remain at the station for about 30 h. Then the simulated AOD decreases again and the observed visibility increases
15 (Fig. 5).

The dust front reaches Hombori during noon on 7 March. The observed visibility decreases from 16 km to 2 km (Fig. 5). The AOD of run F increases. In contrast to Djanet the visibility remains at low and the AOD at high values for a much longer time period.
20 During the first two days of the simulation period the 2 m temperature is underestimated in both model runs (Fig. 5). Due to the horizontal grid size of 28 km the land use in the model differs from the actual one at Hombori. That explains the underestimation of the 2 m temperature (see Sect. 5.2). After the dust front passed the station the observed daily temperature range is reduced by more than 4 K. Like in Djanet this
25 reduction is reproduced by run F, but at the end of the simulation period it is overestimated (Table 4).

Surprisingly, at both stations the simulated temperature of run F is higher than the one of run CTRL during night and day. One would expect that the reduction in surface downward shortwave radiative flux due to absorption and scattering of radiation should

induce a decrease in near surface temperature during noon. This behaviour will be discussed in more detail in Sect. 5.2.

4.4 Comparisons with flux measurements at Niamey

Detailed measurements of the radiative fluxes at the surface were carried out at the ARM Mobile Facility (hereafter ARM-MF) in Niamey, Niger (13.52° N, 2.11° E). The deployment of the ARM-MF was part of the RADAGAST (*R*adiative *A*tmospheric *D*ivergence Using *A*RM Mobile Facility, *G*ERB Data, and *A*MMA *St*ations) project (Miller and Slingo, 2007).

The time series of observed and modelled AOD in Niamey between 5 March, 00:00 UTC and 10 March 2006, 00:00 UTC is shown in Fig. 6a. Slingo et al. (2006) made retrievals of the AOD from data obtained with the Multi-Filter Rotating Shadow-band Radiometer (MFRSR). They derived the aerosol optical properties from MFRSR observations by using an updated version of the retrieval technique described by Kassianov et al. (2005). We used the retrievals at 415 nm of Slingo et al. (2006, Fig. 2) for a comparison with the modelled AOD at 450 nm for run F and CTRL (Fig. 6a).

The observation shows that the dust front arrived in Niamey on 7 March at noon whereas the simulation of the AOD shows a delay of approximately 5 h. The simulated AOD is too low during the first two days after the passage of the front and the observed maximum is not captured in the simulations. Milton et al. (2008) found similar differences between observations and model results for the station at Niamey. They suppose that the reason could be poorly modelled dust sources, an incorrect soil moisture state, or deficiencies in the modelled near surface wind. These reasons would hold for our model runs as well. Moreover, we would add uncertainties of the simulated size distributions, mineralogical composition, and consequently the obtained optical properties of the dust particles. Observed and simulated AOD of run F are in a good agreement on 9 March.

Figure 6b shows the daily cycles of measured and simulated downward shortwave radiative flux at the surface. The observed flux decreased due to the presence of

mineral dust particles at noon of 7 March. As a result of the temporal delay of the modelled dust front the decrease of the surface downward shortwave radiative flux is reproduced in run F with a delay of one day. On 9 March the simulated and the observed AOD values are similar and also the simulated and the observed surface downward shortwave radiative flux are in a good agreement. With prevailing cloud free conditions the flux stays constant from day to day in run CTRL. In this run the surface downward shortwave radiative flux is overestimated by more than 300 W m^{-2} after the passage of the dust front.

Slingo et al. (2006) showed that most of the surface downward shortwave radiative flux is attributed to the diffuse component. Our simulation underestimates the diffuse flux and overestimates the direct flux (Stanelle, 2008). One reason for these deviations could be that the observed aerosol population has a larger single scattering albedo than our simulated ones. This could be caused by a smaller imaginary part of the refractive index or by smaller particles.

The observed upward longwave flux is larger than the simulated one because the observed temperature is higher than the simulated one (Fig. 6f). After the passage of the cold front the observed downward longwave flux is increasing although the observed temperature is decreasing (Fig. 6c, f). This can be attributed to the mineral dust and is reproduced by the results of run F. The increase in longwave radiation is slightly overestimated by the model results. In contrast the temperature and simultaneously the downward flux of longwave radiation are decreasing in run CTRL. The different behaviour clearly demonstrates the effect of the mineral dust particles on the longwave downward flux.

Figure 6d shows the simulated surface radiation budget at Niamey for five consecutive days. The surface radiation budget is given by the sum of net shortwave and net longwave radiative fluxes. Before the arrival of the dust front the simulated surface radiation budget is higher than the observed one during daytime hours. This is caused by the underestimation of the simulated upward longwave flux due to the underestimation of the temperature. The reason for the underestimation of the temperature is given

below.

After the arrival of the dust front a reduced surface radiation budget is observed during the day. On 9 March the simulated AODs of run F are in good agreement with the observed ones. At that day the observed and the simulated reduction of the surface radiation budget during daytime caused by mineral dust (e.g. 5 March) are comparable (observed: $150\,W\,m^{-2}$, simulated: $160\,W\,m^{-2}$). However, in run F the observed surface radiation budget is overestimated during daytime and underestimated during night time before the passage of the dust front. After the passage it is overestimated during night time. There are several reasons for the overestimation during daytime. One reason is the underestimation of upward shortwave flux due to differences between the real surface albedo and the one that was used in the model. Another reason is the overestimation in the downward longwave flux and of the radiative balance during night and day as well.

The overestimation of the surface radiation budget should lead to an overestimation of the surface temperature. However, the surface temperature is underestimated by the model. Figure 6e shows the temporal development of the observed and the simulated latent heat flux. It is obvious that the simulated fluxes are much higher than the observed ones. This is caused by the resolution of our model. While the ARM mobile facility was placed at bare soil in our model runs savannah type vegetation is present at the corresponding grid point. This results in an overestimation of the simulated latent heat flux by the model. Apart from that discrepancy, which we expect to be same for both runs, we can use the observations and the results of the simulation to compare the effects caused by mineral dust. We calculated the observed and the simulated daily temperature range for each day (Table 5). The maximum temperature decreases in run F and run CTRL during 7–8 March. As for Djanet and Hombori the temperature decrease of run CTRL at Niamey is due to the cold front. When the simulated dust front has reached the station the results of run F and CTRL starts to differ. Especially during night much higher temperatures are simulated in run F. This is caused by an increased downward longwave flux due to the mineral dust particles. In agreement with

the observations the maximum temperature in run F stays constant after the mineral dust has reached the station whereas it continues to decrease in run CTRL. Another remarkable effect is a distinct decrease in the daily temperature range. After the arrival of the dust front the daily temperature range is strongly overestimated by neglecting the influence of dust particles on radiative fluxes (run CTRL). A similar behaviour was already found for the station Hombori.

5   Discussion of the model results

Based on our model results we will quantify the impact of mineral dust on the radiative fluxes, the temperature and the feedback between dust particles and their emissions in more detail.

5.1   Impact of mineral dust particles on radiative fluxes

We calculated the differences in net radiative flux (ΔF) caused by mineral dust between the results of runs F and CTRL at 12 UTC at the surface. Based on other studies, ΔF/AOD is called the dust forcing efficiency (e.g. Helmert et al., 2007). Close to source areas in southern Sahara Helmert et al. (2007) found a dust forcing efficiency of $-196\,\mathrm{W\,m^{-2}}$ (AOD = 1, at 500 nm) for particles with high single scattering albedo and $-220\,\mathrm{W\,m^{-2}}$ for particles with a lower single scattering albedo. Averaged over northern Sahara they found $-81\,\mathrm{W\,m^{-2}}$ and $-85\,\mathrm{W\,m^{-2}}$, respectively. Fouquart et al. (1987) found a dust forcing efficiency of $-145\,\mathrm{W\,m^{-2}}$ (AOD = 1, at 550 nm) during a field campaign near Niamey. Mallet et al. (2009) determined similar numbers.

The dependency of ΔF on AOD at 450 nm for our model results is shown in Fig. 7 for 12:00 UTC for all grid points with an AOD greater than 0.1. We found an average forcing efficiency of $-130\,\mathrm{W\,m^{-2}}$ for the net shortwave flux at the surface.

In contrast to the linear behaviour in ratio of ΔF and AOD for the net shortwave flux at the surface, we found a nonlinear relation between the net longwave flux and AOD

and ΔF levels out at about 150 W m^{-2} (Fig. 7). This is in good agreement with the value determined by Milton et al. (2008).

Helmert et al. (2007) determined a shortwave dust forcing efficiency at the top of the atmosphere (TOA) of -121 W m^{-2} close to the source areas and -55 W m^{-2} at larger
5 distances. In contrast to that we found at most grid points positive values. Figure 7 shows the correlation of ΔF and the AOD at TOA. The correlation is not as clear as at the surface. However, ΔF is not only determined by the AOD. We correlated ΔF with the surface albedo (not shown here) and obtained a very clear positive correlation. Negative values of ΔF are only found at those grid points where the surface
10 albedo is below 0.27 i.e. over the ocean. This dependency on the surface albedo was already explained by Liao and Seinfeld (1998). In contrast to our simulation Helmert et al. (2007) used the albedo of the operational COSMO version i.e. a maximum albedo below 0.3 whereas in our setup of the model the maximum value is 0.5. This explains the differences in the sign of the shortwave forcing efficiency.

15 Haywood et al. (2005) applied the UK Met Office Unified Model and found discrepancies between modelled and observed longwave radiative flux on TOA above the Saharan heat low. They identified the lack of mineral dust in the model as a major reason of this systematic error. They got an overestimation in outgoing longwave radiation by cloud free conditions of up to 50 W m^{-2} (daily mean) which implies an underestima-
20 tion of net longwave flux on TOA. They determined a longwave dust forcing efficiency of 20.6 W m^{-2} at TOA. The maximum was 30.3 W m^{-2} and the minimum 13.8 W m^{-2}. Close to the source areas the dust forcing efficiency was determined as 29 W m^{-2} by Helmert et al. (2007). For the dust outbreak in March 2006 Slingo et al. (2006) derived the outgoing longwave radiation from the GERB broadband radiometer. They show that
25 the net longwave radiation at TOA increased by 30 W m^{-2}. Mallet et al. (2009) found a positive effect of dust aerosols on net longwave radiation on TOA over the entire West Africa region during 9–12 March 2006 (at noon). They determined an increase between 20 and 50 W m^{-2}.

The relationship of net longwave forcing and AOD at TOA at 12:00 UTC for our model

Printer-friendly Version

Interactive Discussion

results is not as pronounced as for net longwave fluxes at surface (Fig. 7). The mean increase for a dust layer with an AOD (450 nm) of 1 is 26.4 W m^{-2}. The reduction of outgoing longwave radiation at TOA can be caused by a reduction in surface temperature due to the decrease of downward shortwave radiation or by the absorption and
5 re-emission of longwave radiation by the dust plume.

5.2 Effects on the temperature

We have shown in Sects. 4.3 and 4.4 that the dust plume causes an increase of the 2 m temperature during the day. We will discuss this behaviour in more detail on the basis of the dust storm in March 2006. During this dust storm the dust particles were
10 located in the boundary layer.

The energy available at the ground is reduced due to the reduction of the radiative balance during day. According to this the surface temperature should decrease. This is the case during the first simulation day. After 15 h simulation time, during afternoon on 5 March, the surface temperature decreases by 0.2 K to 3 K due to the dust plume
15 (Fig. 8). Changes in temperature in regions without dust particles, e.g. in the region of the Intertropical Convergence Zone, are due to changes in cloud cover. The maximum decrease in 2 m temperature is about 3 K. Helmert et al. (2007) determined a reduction in 2 m temperature of 3 K for more reflecting particles and of 3.3 K for more absorbing particles close to source areas. Milton et al. (2008) determined a reduction in 1.5 m
20 temperature between 0.5 K and 2 K for 8 March 2008. Tulet et al. (2008) found a reduction in surface temperature of more than 6 K in some places during the end of the dust storm in March 2006.

The 2 m temperature in run F is higher than in run CTRL during the night of 5–6 March (Fig. 8). The nocturnal cooling is reduced by up to 5 K in run F. Tegen et
25 al. (2006) determined a reduction of nocturnal cooling of approximately 1 K due to a dust plume in the Bodélé Depression. Pérez et al. (2006) found a reduction in near surface temperature during both day and night.

During the next day the temperature in run F is higher than in run CTRL in areas that

Full Screen / Esc

Printer-friendly Version

Interactive Discussion

were influenced by the dust plume during the night before or which are affected by the advection of heated (by dust particles) air (Fig. 8). This is caused by a combination of reduction of nocturnal cooling and the warming of the air layer due to the absorption of radiation by the mineral dust particles. Due to the reduction of shortwave radiation at
5 the surface the temperature difference during day is not as high as during night.

During the dust episode that occurred over West Africa in June 2007 the dust layer is elevated through isentropic lifting in the intertropical discontinuity zone (Stanelle, 2008). Figure 9 shows the AOD and the 2 m temperature difference between run F and CTRL for 21 June 2007, 15:00 UTC. Figure 10 shows a vertical cross section of the mass
10 concentration of mineral dust and of the temperature difference along the line marked in Fig. 9 for the same point in time. An increase in near surface temperature occurs in areas where the dust layer is located close to the surface as it was the case during the episode in March 2006. A decrease in near surface temperature is found in those areas where an elevated dust layer occurs. In this case the cooling is also reduced
15 during night. The decrease in nocturnal cooling does not lead to an increase in near surface temperature during daytime in this case. The reduction of downward shortwave radiation during the day causes a decrease of the temperature in the boundary layer. The air layer which is heated by absorption of radiation by dust particles is above the boundary layer. This shows that the location and the vertical extension of the dust
20 plume determine the effect on 2 m temperature.

Due to the different influence of an elevated and a near surface dust layer on the surface temperature during day, the meridional temperature gradient at the surface increases (Fig. 9). The North becomes warmer and the South colder due to the radiative effect of the dust layer. This increase in the meridional temperature gradient results
25 in an intensification of the secondary circulation in the region of the intertropical front (Stanelle, 2008). The upward motion is increased by a factor of 2 in run F in comparison to run CTRL on 21 June, 21:00 UTC.

5.3 Changes of the emission rate of dust particles

Changes in the state of the atmosphere induce modifications in the emission rate of dust particles. As discussed in Sect. 2.1 the emission of dust particles depend on the friction velocity and the soil properties. The soil properties are fixed in time but friction velocity alters due to changes in wind speed and thermal stability.

The emission rate of dust particles has a diurnal cycle. The simulated emission rates reach their maximum around noon and their minimum around 22:00 UTC. Caused by the diurnal cycle of the friction velocity the simulated dust emission is low during night and high during day. At noon of 7 March 2006 the total emission rate in the model area reaches a maximum of more than $100\,t\,s^{-1}$. During night the total emission rate in run F is larger than in run CTRL by a factor of 2. The thermal stability at the surface is reduced in run F in comparison to run CTRL during night. This reduction is induced by the decrease in nocturnal cooling due to the dust layer. During noon the mean wind velocity decreases slightly. This results in a decrease of dust emission. Integrated over the entire simulation period (5–10 March) the total emission flux is about 16% higher in run F than in run CTRL.

21 June is the day with the most intensive total dust emission flux in the simulation area during the dust episode in June 2007. During that day the increase in dust emission in run F in comparison to run CTRL is between 12 % (noon) and 100% (during night). Integrated over the whole simulation period (19–24 June) and the simulation area the increase in dust emission is 25% when considering the feedback between dust particles and radiative fluxes.

6 Conclusions

We extend the fully online coupled model system COSMO-ART (Vogel et al., 2009) to treat mineral dust particles and their influence on the radiative fluxes.

We compared our model results with observations for the dust event in March 2006.

The location of the dust front was captured by our model, only at some stations the simulated dust front arrived a few hours later than the observed one. The comparison with measurements of radiative fluxes at Niamey show a reasonable agreement between modelled and observed radiative fluxes when the influence of dust particles on radiative fluxes is considered in the model run. The downward shortwave radiation at the surface is well reproduced by run F in Niamey. The downward longwave radiation at the surface increases after the passage of the dust front in both observation and run F. The rise in downward longwave radiation is overestimated in run F. After the passage of the dust front the observed diurnal temperature range is reduced. This is reproduced by the feedback run. The fact that even the model run without the consideration of the feedback between mineral dust particles and radiative fluxes reproduces the observed decrease in 2 m temperature after the arrival of the dust front shows that the initial decrease is caused by the passage of the cold front and not by the dust particles.

We analysed the radiative efficiency of dust particles. For net shortwave radiation at the surface we found a radiative efficiency of $-129\,\mathrm{W\,m^{-2}}$. At TOA the influence of dust particles depends strongly on surface albedo. In this case we did not find a clear relationship between AOD and changes in net shortwave radiative fluxes. At the surface the increase of the net longwave radiative fluxes is about $79\,\mathrm{W\,m^{-2}}$ for a dust layer with an AOD of 1. If such a dust layer is present the increase of net longwave radiative fluxes is approximately $26\,\mathrm{W\,m^{-2}}$ at TOA.

We found that mineral dust particles are able to cause both, a decrease and an increase in near surface temperature during the day. They cause a decrease in regions where dust particles are freshly emitted or an elevated dust layer is present. The decrease in 2 m temperature is up to 4 K. The 2 m temperature increases if the dust layer is attached to the surface and is present at least since the day before. The increase is caused by a combination of the reduction of nocturnal cooling and the warming of the air layer due to the absorption of radiation by the mineral dust particles. Due to the reduction of shortwave radiation at the surface the temperature difference during day is not as high as during night.

The feedback between mineral dust particles and radiative fluxes leads to changes in the physical state of the atmosphere. Changes in the wind field and the thermal stability induce modifications in the emission flux of dust particles. We found an increase in the total emission flux of dust particles by about 16% during the dust storm in March 2006
5 and 25% during the dust episode in June 2007. The main increase takes place during night. In wide areas the emission flux decreases slightly during the day. Our results demonstrate the importance to use online coupled models to determine the emission flux and the radiative effect of mineral dust particles.

Based on our model results we conclude that these processes should be included in
10 numerical weather forecast models.

References

Ackermann, A. S., Toon, O. B., Stevens, D. E., Heymsfield, A. J., Ramanathan, V., and Welton, E. J.: Reduction of tropical cloudiness by soot, Science, 288, 1042–1047, 2000.
Albrecht, B. A.: Aerosols, cloud microphysics, and fractional cloudiness, Science, 245, 1227–
25 1230, 1989.
Alfaro, S. C. and Gomes, L.: Improving the large-scale modelling of the saltation flux of soil particles in presence of nonerodible elements, J. Geophys. Res., 100, 16357–16366, 1995.
Alfaro, S. C. and Gomes, L.: Modeling mineral aerosol production by wind erosion: Emis-

I◀ | ▶I

◀ | ▶

Back | Close

Full Screen / Esc

sion intensities and aerosol size distributions in source areas, J. Geophys. Res., 106(D16), 18075–18084, 2001.

Bohren, C. F. and Huffman, D. R.: Absorption and Scattering of Light by Small Particles, John Wiley and Sons, New York, USA, 1983.

5 Callot Y., Marticorena, B., and Bergametti, G.: Geomorphologic approach for modelling the surface features of arid environments in a model of dust emissions: application to the Sahara desert, Geodinami. Acta, 13, 245–270, 2000.

Chameides, W. L., Lou, C., Saylor, R., Streets, D., Huang, Y., Bergin, M., Giorgi, F.: Correlation between model-calculated anthropogenic aerosols and satellite-derived cloud optical depth:

10 Indication of indirect effect?, J. Geophys. Res., 107(D10), 4085, doi:10.1029/2000JD000208, 2002.

Charlson, R. J., Schwartz, S. E., Hales, J. M., Cess, R. D., Coakley, J. A., Hansen, J. E., and Hofmann, D. J.: Climate forcing by anthropogenic aerosols, Science, 255, 423–430, 1992.

Chen, S., Kuo, Y., Ming, W., and Ying, H.: The effect of dust radiative heating on low-level

15 frontogenesis, J. Atmos. Sci., 52, 1414–1420, 1994.

Cook, J. and Highwood, E. J.: Climate response to tropospheric absorbing aerosols in an intermediate general-circulation model, Q. J. Roy. Meteor. Soc., 130, 175–191, 2004.

European Centre for Medium-Range Weather Forecasts, IFS documentation, technical report, Reading, UK, available online at http://www.ecmwf.int/research/ifsdocus/, 2004.

20 Fécan, F., Marticorena, B., and Bergametti, G.: Parameterisation of the increase of the Aeolian erosion threshold wind velocity due to soil moisture for arid and semi-arid areas, Ann. Geophys., 17, 149–157, 1999, http://www.ann-geophys.net/17/149/1999/.

Formenti, P., Rajot, J. L., Desboeufs, K., Chevaillier, S., Caquineau, S., Nava, S., Chiari, M., Triquet, S., Journet, E., Gaudichet, A., Alfaro, S., Haywood, J., Coe, H., and Highwood,

25 E.: Regional variability of the composition of mineral dust from western Africa: Results from the AMMA SOP0/DABAX and DODO field campaigns, J. Geophys. Res, 113, D00C13, doi:10.1029/2008JD009903, 2008.

Fouquart, Y., Bonnel, B., Brogniez, G., Buriez, J. C., Smith, L., Morcrette, J. J., and Cerf, A.: Observations of Saharan aerosols: Results of ECLATS field experiment. Part II: broadband

30 radiative characteristics of aerosols and vertical radiative flux divergence, J. Clim. Appl. Meteorol., 26, 38–52, 1987.

Gillies, J. A., Nickling, W. G., and McTainsh, G. H.: Dust concentration and particle-size characteristics of an intense dust haze event: Inland delta region, Mali, West Africa, Atmos.

Feedback between dust particles and atmospheric processes

T. Stanelle et al.

Title Page

Abstract	Introduction
Conclusions	References
Tables	Figures

◀◀ ▶▶

◀ ▶

Back Close

Full Screen / Esc

Printer-friendly Version

Interactive Discussion

Environ., 30, 1081–1090, 1996.

Gomes, L., Rajot, J. L., Alfaro, S. C., and Gaudichet, A.: Validation of a dust production model from measurements performed in semi-arid agricultural areas of Spain and Niger, Cantena, 57, 257–271, 2003.

5 Grini, A., Tulet, P., and Gomes, L.: Dusty weather forecasts using the MesoNH mesoscale atmospheric model, J. Geophys. Res., 111, D19205, doi:10.1029/2005JD007007, 2006.

Haywood, J. M., Allan, R. P., Culverwell, I., Slingo, T., Milton, S., Edwards, J., and Clerbaux, N.: Can desert dust explain the outgoing longwave radiation anomaly over the Sahara during July 2003?, J. Geophys. Res., 102, 6831–6864, 2005.

10 Heinold, B., Helmert, J., Hellmuth, O., Wolke, R., Ansmann, A., Marticorena, B., Laurent, B., and Tegen, I.: Regional modeling of Saharan dust events using LM-MUSCAT: Model description and case studies, J. Geophys. Res., 112, D11204, doi:10.1029/2006JD007443, 2007.

Helmert, J., Heinold, B., Tegen, I., Hellmuth, O., and Wendisch, M.: On the direct and semi-

15 direct effect of Saharan dust over Europe: A case study, J. Geophys. Res., 112, D13208, doi:10.1029/2006JD007444, 2007.

Hoose, C., Lohmann, U., Erdin, R., and Tegen, I.: The global influence of dust mineralogical composition on heterogeneous ice nucleation in mixed-phase clouds, Environ. Res. Lett., 3, 025003, doi:10.1088/1748-9326/3/2/025003, 2008.

20 IPCC, Climate Change 2007: The Physical Basis, edited by: Forster, P., Ramaswamy, V., Artaxo, P., Berntsen, T., Betts, R., Fahey, D. W., Haywood, J., Lean, J., Lowe, D. C., Myhre, G., Nganga, J., Prinn, R., Raga, G., Schulz, M., and Van Dorland, R.: Changes in Atmospheric Constituents and in Radiative Forcing., Cambridge University Press, Cambridge, UK and New York, NY, USA, 129–234, 2007.

25 Johnson, B. T., Shine, K. P., and Forster, P. M.: The semi-direct aerosol effect: Impact of absorbing aerosols on maritime stratocumulus, Q. J. Roy. Meteor. Soc., 130, 1407–1422, 2004.

Karyampudi, V. M. and Carlson, T. N.: Analysis and numerical simulations of the Saharan air layer and its effects on easterly wave disturbances, J. Atmos. Sci., 45, 3102–3136, 1988.

30 Kassianov, S. I., Barnard, J. C., and Ackerman, T. P.: Retrieval of aerosol microphysical properties using surface Multi Filter Rotating Shadowband Radiometer (MFRSR) data: Modeling and observations, J. Geophys. Res., 110, D09201, doi:10.1029/2004JD005337, 2005.

Kischa, P., Alpert, P., Barkan, J., Kirchner, I., and Machenhauer, B.: Atmospheric response

Feedback between dust particles and atmospheric processes

T. Stanelle et al.

Printer-friendly Version

Interactive Discussion

to Saharan dust deduced from ECMWF reanalysis (ERA) temperature increments, Tellus B, 55, 901–913, 2003.

Knippertz, P. and Fink, A. H.: Synoptic and dynamic aspects of an extreme springtime Saharan dust outbreak, Q. J. R. Meteorol. Soc., 132, 1153–1177, 2006.

5 Lacis, A. A. and Mishchenko, M. I.: Climate forcing, climate sensitivity, and climate response: A radiative modelling perspective on atmospheric aerosols., in Aerosol Forcing of Climate: Report of the Dahlem Workshop on Aerosol forcing of Climate, edited by R. Charlson and J. Heintzenberg, John Wiley Sons., Chichester, UK, New York, USA and Berlin, Germany, 11–42, 1995.

10 Liao, H. and Seinfeld, J. H.: Radiative forcing by mineral dust aerosols: sensitivity to key variables, J. Geophys. Res, 103, 31637–31645, 1998.

Lu, H. and Shao, Y.: A new model for dust emission by saltation bombardment, J. Geophys. Res., 104, 16827–16841, 1999.

Mallet, M., Tulet, P., Serça, D., Solmon, F., Dubovik, O., Pelon, J., Pont, V., and Thouron, O.:
15 Impact of dust aerosols on the radiative budget, surface heat fluxes, heating rate profiles and convective activity over West Africa during March 2006, Atmos. Chem. Phys., 9, 7143–7160, 2009, http://www.atmos-chem-phys.net/9/7143/2009/.

Marsham, J. H., Parker, D. J., Grams, C. M., Taylor, C. M., and Haywood, J. M.: Uplift of Saharan dust south of the intertropical discontinuity, J. Geophys. Res., 113, D21102,
20 doi:10.1029/2008JD009844, 2008.

Martin, J. H.: Glacial-interglacial CO_2 change: The iron hypothesis, Paleoceanography, 5, 1–13, 1990.

Marticorena, B., Bergametti, G., Aumont, B., Callot, Y., N'Doumé, C., and Legrand, M.: Modeling the atmospheric dust cycle: 2-Simulations of Saharan dust sources, J. Geophys. Res.,
25 102, 4387–4404, 1997.

Miller, M. A. and Slingo, A.: The ARM Mobile Facility and its first international deployment: measuring radiative flux divergence in West Africa, B. Am. Meteorol. Soc., 88, 1229–1244, 2007.

Miller, R. L., Perlwitz, J., and Tegen, I.: Feedback upon dust emission by dust radiative forcing through the planetary boundary layer, J. Geophys. Res., 109, D24209,
30 doi:10.1029/2004JD004912, 2004.

Milton, S. F., Greed, G., Brooks, M. E., Haywood, J., Johnson, B., Allan, R. P., and Grey, W. M. F.: Modelled and observed atmospheric radiation balance during West Africa dry season:

Feedback between dust particles and atmospheric processes

T. Stanelle et al.

Role of mineral dust, biomass burning aerosol, and surface albedo, J. Geophys. Res., 113, D00C02, doi:10.1029/2007JD009741, 2008.

Mishchenko, M. I., Travis, L. D., and Lacis, A. A.: Scattering, Absorption, and Emission of Light by Small Particles, Cambridge University Press, Cambridge, UK, 2002.

5   Myhre, G., Grini, A., Haywood, J. M., Stordal, F., Chatenet, B. C, B., Tanré, D., Sundet, J. K., Jostein, K., and Isaksen, I. S. A.: Modeling the radiative impact of mineral dust during the Saharan Dust Experiment (SHADE) campaign, J. Geophys. Res, 108(D18), 8579, doi:10.1029/2002JD002566, 2003.

Nenes, A., Contant, W. C., and Seinfeld, J. H.: Black carbon radiative heating effects on cloud
10   microphysics and implications for the aerosol indirect effect- 2. cloud microphysics, J. Geophys. Res., 107, 4605, doi:10.1029/2002JD002101, 2002.

Nicholson, S. E., Tucker, C. J., and Ba, M. B.: Desertification, drought, and surface vegetation: An example from the West African Sahel, B. Am. Meteorol. Soc., 79, 815–829, 1998.

Nickovic, S., Kallos, G., Papadopoulos, A., and Kakaliagou, O.: A model for prediction of desert
15   dust cycle in the atmosphere, J. Geophys. Res., 106, 18113–18129, 2001.

Patterson, E. M., Gillette, D. A., and Stockton, B. H.: Complex Index of Refraction between 300 and 700 nm for Saharan Aerosols, J. Geophys. Res., 82, 3153–3160, 1977.

Péez, C., Nickovic, S., Pejanovic, G., Baldasano, J. M., Özsoy, E.: Interactive dust-radiation modeling: A step to improve weather forecasts, J. Geophys. Res., 111, D16206,
20   doi:10.1029/2005JD006717, 2006.

Perlwitz, J., Tegen, I., and Miller, R. L.: Interactive soil dust aerosol model in the GISS GCM 1. Sensitivity of the soil dust cycle to radiative properties of soil dust aerosols, J. Geophys. Res., 106, 18167–18192, 2001.

Petzold, A., Rasp, K., Weinzierl, B., Esselborn, M., Hamburger, T., Dörnbrack, A., Kandler, K.,
25   Schütz, L., Knippertz, P., Fiebig, M., and Virkkula, A.: Saharan dust absorption and refractive index and from aircraft-based observations during SAMUM 2006, Tellus B, 61B, 118–130, 2009.

Prospero, J. M.: Long-term measurements of the transport of African mineral dust to the southeastern United States: Implications for regional air quality, J. Geophys. Res., 104, 15917–
30   15928, 1999.

Redelsperger, J. L., Thorncroft, C. D., Diedhiou, A., Lebel, T., Parker, D. J., and Polcher, J.: African Multidisciplinary Analysis An International Research Project and Field Campaign, American Meteorological Society, 1739–1746, 2006.

Feedback between dust particles and atmospheric processes

T. Stanelle et al.

Title Page

Abstract	Introduction
Conclusions	References
Tables	Figures

◄◄   ►►

◄   ►

Back   Close

Full Screen / Esc

Printer-friendly Version

Interactive Discussion

Ritter, B. and Geleyn, J.-F.: A Comprehensive Radiation Scheme for Numerical Weather Prediction Models with Potential Applications in Climate Simulations, Mon. Weather Rev., 120, 303–325, 1992.

Rosenfeld, D.: Suppression of rain and snow by urban and industrial air pollution, Science, 287, 1793–1796, 2000.

Schwartz, S. E.: The whitehouse effect – shortwave radiative forcing of climate by anthropogenic aerosols: An overview, J. Aerosol Science, 27, 359–382, 1996.

Seinfeld, J. H. and Pandis, S.: Atmospheric Chemistry and Physics., John Wiley & Sons, Inc., ISBN-10: 0471178160, 1326 pp., 1998.

Shettle, E. P. and Fenn, R. W.: Models for Aerosols of the Lower Atmosphere and the Effects of Humidity Variations on Their Optical Properties, AFGL-TR-79-0214, 12, ADA085951, 1979.

Sinyuk, A., Torres, O., and Dubovik, O.: Combined use of satellite and surface observations to infer the imaginary part of refractive index of Saharan dust, Geophys. Res. Lett., 30, 1081, doi:10.1029/2002GL016189, 2003.

Slingo, A., Ackerman, T. P., Allan, R. P., Kassianov, E. I., McFarlane, S. A., Robinson, G. J., Barnard, J. C., Miller, M. A., Harries, J. E., Russell, J. E., and Dewitte, S.: Observations of the impact of a major dust storm on the atmospheric radiation balance, Geophys. Res. Lett., 33(24), L24817, doi:10.1029/2006GL027869, 2006.

Sokolik, I. N. and Toon, O. B.: Direct radiative forcing by anthropogenic airborne mineral aerosols, Nature, 381, 681–683, 1996.

Sokolik, I. N. and Toon, O. B.: Incorporation of mineralogical composition into models of the radiative properties of mineral aerosol from uv to ir wavelength, J. Geophys. Res., 104, 9423–9444, 1999.

Stanelle, T.: Wechselwirkungen von Mineralstaubpartikeln mit thermodynamischen und dynamischen Prozessen in der Atmosphäre über Westafrika, Dissertation, Institut für Meteorologie und Klimaforschung der Universität Karlsruhe, 157 pp., 2008.

Steppeler, J., Doms, G., Schättler, U., Bitzer, H., Gassmann, A., Damrath, U., and Gregoric, G.: Meso gamma scale forecasts using the nonhydrostatic model LM, Meteorol. Atmos. Phys., 82, 75–96, 2002.

Swap, R., Garstang, M., Greco, S., Talbot, R., and Kållberg, P.: Saharan dust in the Amazon Basin, Tellus, Ser. B, 44, 133–149, 1992.

Tanre, D., Geleyn, J.-F., and Slingo, J. M.: First results of the introduction of an advanced aerosol-radiation interaction in the ECMWF low resolution global model, In Proc. Of the

Feedback between dust particles and atmospheric processes

T. Stanelle et al.

Title Page

Abstract	Introduction
Conclusions	References
Tables	Figures

|◄ ►|

◄ ►

Back Close

Full Screen / Esc

Printer-friendly Version

Interactive Discussion

Meeting of Experts on Aerosol and Their Climatic Effects, VA. WMO and International Association of Meteorology and Atmospheric Physics, Williamsburg, 133–177, 1984

Tegen, I., Lacis, A. A., and Fung, I.: The influence on climate forcing of mineral aerosols from disturbed soils, Nature, 380, 419–422, 1996.

Tegen, I., Heinold, B., Todd, M., Helmert, J., Washington, R., and Dubovik, O.: Modeling soil dust aerosol in the Bodélé Depression during BoDEx campaign, Atmos. Chem. Phys., 6, 4171–4211, 2006

Tegen, I., Harrison, S. P., Kohfeld, K., Prentice, I. C., Coe, M., and Heimann, M.: Impact of vegetation and preferential source areas on global dust aerosol: Results from a model study, J. Geophys. Res., 107(D21), 4576, doi:10.1029/2001JD000963, 2002

Tulet, P., Mallet, M., Pont, V., Pelon, J., and Boone, A.: The 7–13 March 2006 dust storm over West Africa: Generation, transport, and vertical stratification, J. Geophys. Res., 113, D00C08, doi:10.1029/2008JD009871, 2008.

Twomey, S. A., Piepgrass, M., and Wolfe, T. L.: An assessment if the impact of pollution on global cloud albedo, Tellus, Ser. B, 36, 356–366, 1984.

Vogel, B., Hoose, C., Vogel, H., and Kottmeier, C.: A Model of dust transport applied to the Dead Sea Area, Meteorol. Z., 6, 611–624, 2006.

Vogel, B., Vogel, H., Bäumer, D., Bangert, M., Lundgren, K., Rinke, R., Stanelle, T.: The comprehensive model system COSMO-ART – Radiative impact of aerosol on the state of the atmosphere on the regional scale, Atmos. Chem. Phys., 9, 8661–8680, 2009, http://www.atmos-chem-phys.net/9/8661/2009/.

White, B. R.: Soil transport by winds on Mars, J. Geophys. Res., 84, 4643-4651, 1979.

Woodward, S.: Modeling the atmospheric life cycle and radiative impact of mineral dust in the Hadley Centre climate model, J. Geophys. Res., 106, 18155–18166, 2001.

Volz, F. E.: Infrared Absorption of Atmospheric Aerosol Substances, J. Geophys. Res., 77, 1017–1031, 1972a.

Volz, F. E.: Infrared Refractive Index of Atmospheric Aerosol Substances, Applied Optics, 11, 755–759, 1972b.

Volz, F. E.: Infrared Optical Constants of Ammonium Sulfate, Saharan Dust, Volcanic Pumice, and Flyash, Appl. Opt., 12, 564–568, 1973.

Yoshioka, M., Mahowald, N. M., Conley, A. J., Collins, W. D., Fillmore, D. W., Zender, C. S., and Coleman, D. B.: Impact of Desert Dust Radiative Forcing on Sahel Precipitation: Relative Importance of Dust Compared to Sea Surface Temperature Variations, Vegetation Changes,

Title Page

Abstract | Introduction

Conclusions | References

Tables | Figures

◄ | ►

◄ | ►

Back | Close

Full Screen / Esc

Printer-friendly Version

Interactive Discussion

and Greenhouse Gas Warming, J. Clim., 20, 1445–1467, doi:10.1175/JCLI4056.1, 2007.

Zender, C. S., Bian, H., and Newman, D.: Mineral dust Entrainment and Deposition (DEAD) model: Description and 1990s dust climatotlogy, J. Geophys. Res., 108(D14), 4416, doi:10.1029/2002JD002775, 2003.

Feedback between dust particles and atmospheric processes

T. Stanelle et al.

Title Page

Abstract | Introduction

Conclusions | References

Tables | Figures

◄ | ►|

◄ | ►

Back | Close

Full Screen / Esc

Printer-friendly Version

Interactive Discussion

Table 1. Classification of 13 different sand types. Each type contains information of up to three size distributions of particles including the median diameter (d_{gs}), the standard deviation (σ_s), and the fraction of erodible surface (fraction) (Chatenet et al., 1996). Additionally information about the residual soil moisture content (w') is given (Fécan et al., 1999).

Soil type	$d_{gs1}, d_{gs2}, d_{gs3}$ in m	$\sigma_{s1}, \sigma_{s2}, \sigma_{s3}$	fraction	w'
Silty fine sand	210E-6, 125E-6, 0	1.8, 1.6, 0	0.625, 0.375, 0	1.05
Medium sand	210E-6, 690E-6, 0	1.8, 1.6, 0	0.2, 0.8, 0	0.12
Coarse sand	0, 690E-6, 0	0, 1.6, 0	0, 1, 0	0
Coarse medium sand	210E-6, 690E-6, 0	1.8, 1.6, 0	0.1, 0.9, 0	0.06
Fine sand	210E-6, 0, 0	1.8, 0, 0	1, 0, 0	0.63
Silty medium sand	210E-6, 690E-6, 125E-6	1.8, 1.6, 1.6	0.3125, 0.3125, 0.375	0.84
Salty medium sand	125E-6, 520E-6, 0	1.6, 1.5, 0	0.2, 0.8, 0	0.8
Salty silt fort	125E-6, 520E-6, 0	1.6, 1.5, 0	0.08, 0.92, 0	0.66
Clayey soil clay	0	0	0	0
Salt waste	125E-6, 520E-6, 0	1.6, 1.5, 0	0.5, 0.5, 0	1.16
Sol agricole	125E-6, 0, 0	1.6, 0, 0	1, 0, 0	1.78
Salty fine sand	125E-6, 520E-6, 210E-6	1.6, 1.5, 1.8	0.1, 0.4, 0.5	0.71
Silty coarse sand	690E-6, 125E-6, 0	1.6, 1.6, 0	0.6, 0.4, 0	0
Other	0, 0, 0	0, 0, 0	0, 0, 0	0

Table 2. Statistical parameters for mineral dust particles after Alfaro and Gomes (1995).

Mode	dg in µm	σ
1	1.7	1.5
2	6.7	1.6
3	14.2	1.7

Title Page

Abstract | Introduction

Conclusions | References

Tables | Figures

◄◄ | ►►

◄ | ►

Back | Close

Full Screen / Esc

Printer-friendly Version

Interactive Discussion

Table 3. Specific extinction coefficient ($\tilde{b}_e$), single scattering albedo ($\tilde{\omega}$), and asymmetry parameter ($\tilde{g}$) derived from Mie-calculations for the three dust modes (1–3) and the eight spectral bands (k) used by COSMO-ART. The values of the specific extinction coefficients are given in $m^2\,g^{-1}$.

k	1	2	3	4	5	6	7	8
λ in µm	1.53–4.64	0.7–1.53	0.25–0.7	20–104.5	12.5–20	8.33–9.01 10.31–12.5	9.01–10.31	4.64–8.33
$\tilde{b}_{e,1,k}$	0.606	0.543	0.481	0.070	0.136	0.178	0.400	0.220
$\tilde{b}_{e,2,k}$	0.293	0.262	0.248	0.086	0.151	0.229	0.306	0.243
$\tilde{b}_{e,3,k}$	0.257	0.232	0.222	0.090	0.157	0.230	0.280	0.239
$\tilde{\omega}_{1,k}$	0.975	0.983	0.890	0.105	0.150	0.409	0.353	0.515
$\tilde{\omega}_{2,k}$	0.949	0.970	0.832	0.226	0.323	0.575	0.476	0.589
$\tilde{\omega}_{3,k}$	0.943	0.967	0.821	0.258	0.367	0.590	0.491	0.594
$\tilde{g}_{1,k}$	0.665	0.668	0.749	0.097	0.198	0.392	0.233	0.659
$\tilde{g}_{2,k}$	0.814	0.737	0.659	0.140	0.307	0.489	0.451	0.779
$\tilde{g}_{3,k}$	0.681	0.746	0.823	0.156	0.345	0.521	0.517	0.798

Table 4. Observed and simulated daily temperature range (DTR) in K for Djanet and Hombori.

	Date				
	5.3.	6.3.	7.3.	8.3.	9.3.
Djanet, observed	14.1	13.4	6.2	14.8	15
Djanet, run F	14.6	13.3	8.3	16.3	16.4
Djanet, run CTRL	14.6	14.2	10.5	16.7	17.4
Hombori, observed	15	13.4	9	11	10.2
Hombori, run F	18.1	16.3	13.1	8.4	6.9
Hombori, run CTRL	18.1	16.4	14.1	15.4	13.5

Full Screen / Esc

Table 5. Observed and simulated daily temperature range (DTR) in K for Niamey.

	Date				
	5.3.	6.3.	7.3.	8.3.	9.3.
Observations	15.5	15.0	11.6	8.6	7.8
run F	15.4	16.1	13.8	10.0	6.5
run CTRL	15.4	16.1	13.8	12.7	13.0
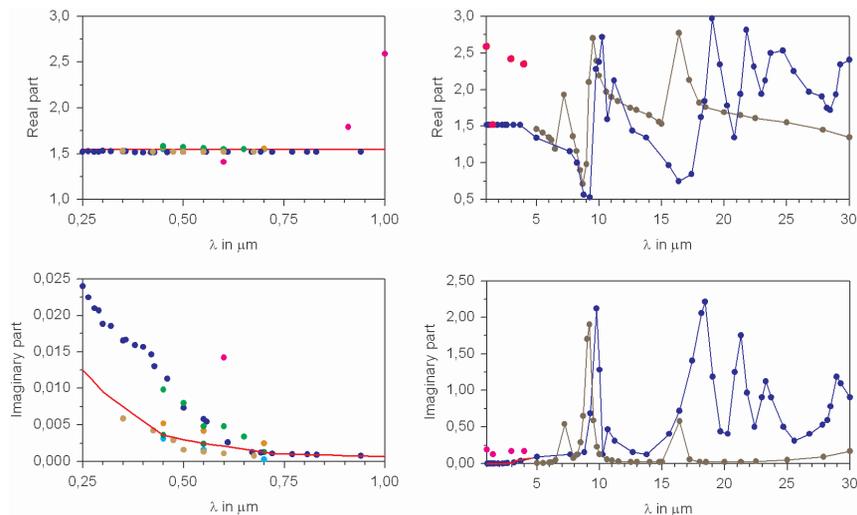
Fig. 1. Refractive indices for mineral dust of different studies (red: values used in run F; blue: Tegen, used in Helmert et al. (2007) and in the longwave spectrum in run F; pink: Volz (1973); brown: Sinyuk et al. (2003); green: Patterson et al. (1977); orange and light blue: Petzold et al. (2009) episodes 1 and 3; grey: Volz (1972a, b) and Shettle and Fenn (1979)).
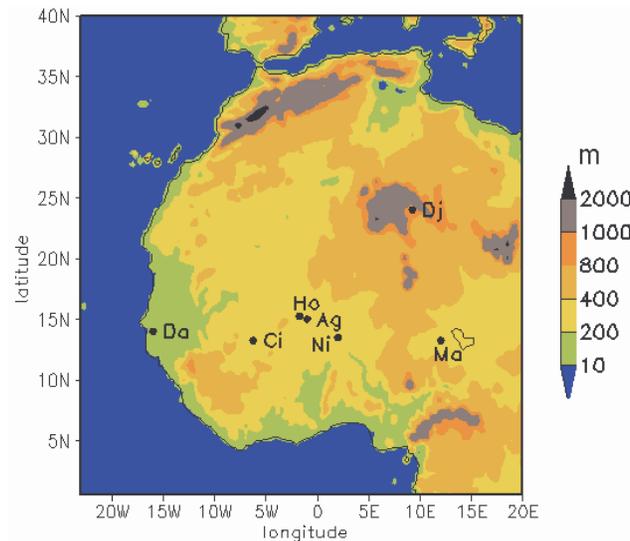
Fig. 2. Model domain and stations used for comparison with model results. (Ag – Agoufou, Ci – Cinzana, Da – Dakar, Dj – Djanet, Ho – Hombori, Ma – Maine Soroa, Ni – Niamey).
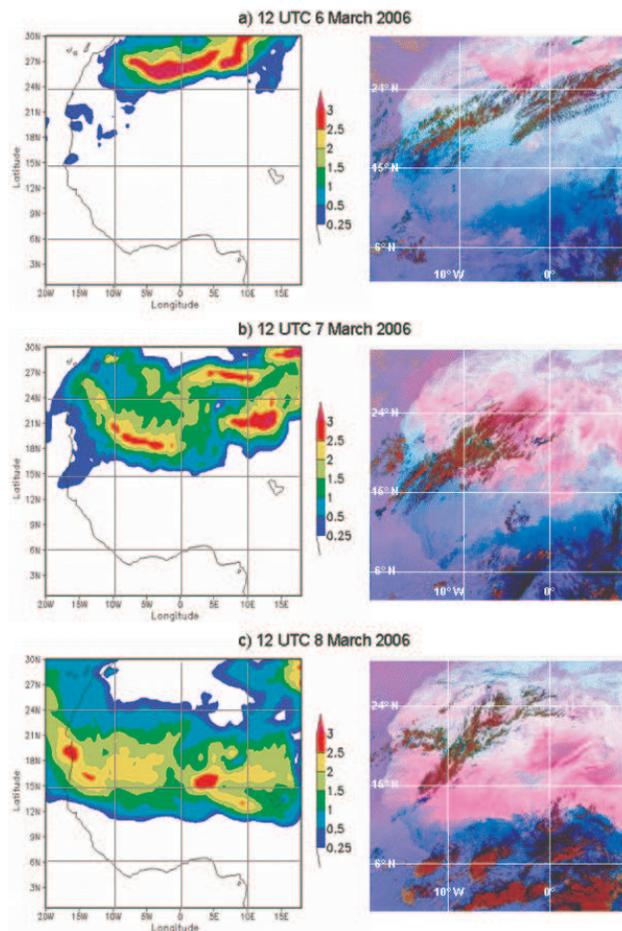
Fig. 3. Simulated AOD at 450 nm of run F (left) and SEVIRI RGB dust product with dust shown in pink and cold high clouds in dark red (right).
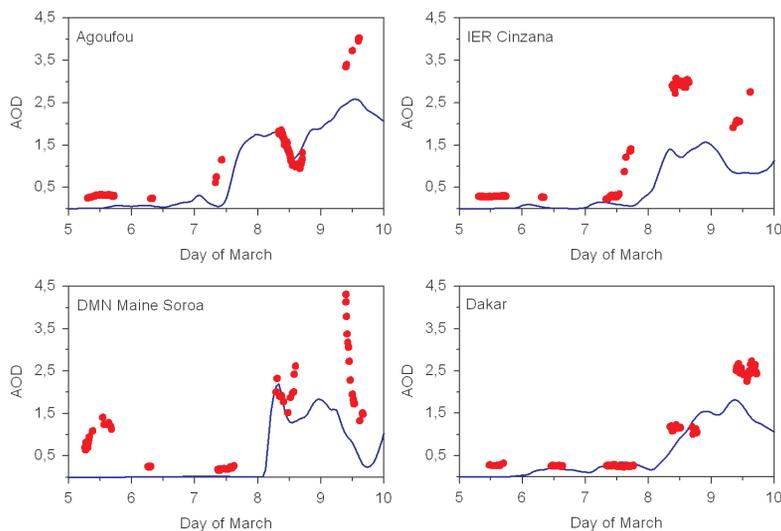
Fig. 4. Simulated (blue) AOD at 450 nm and measured AOD at 440 nm (red) at AERONET stations during 5–10 March 2006.

Fig. 5. Observed visibility and simulated AOD at 450 nm (run F) at Djanet and Hombori during 5–10 March 2006 (left) and corresponding observed and simulated 2 m temperature (right). Observations: red, run F: blue, run CTRL: green.

Fig. 6. Simulated AOD at 450 nm and observed AOD at 415 nm (taken from Slingo et al. (2006), Fig. 2), shortwave downward radiation, longwave downward radiation, net radiation, latent heat flux, and 2 m temperature during 5–10 March 2006 at Niamey. Observations: red, run F: blue, run CTRL: green.

Title Page

Abstract	Introduction
Conclusions	References
Tables	Figures

|◄ | ►|

◄ | ►

| Back | Close |

Full Screen / Esc

Printer-friendly Version

Interactive Discussion
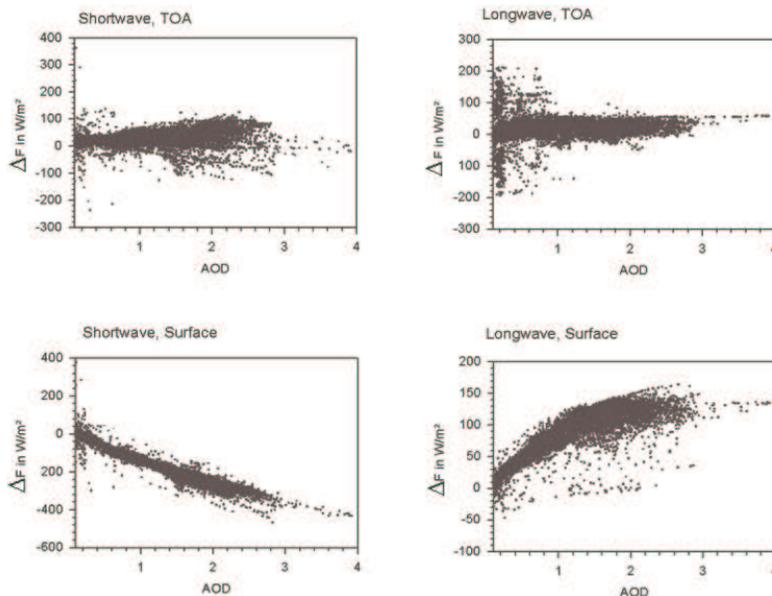
Fig. 7. Difference in shortwave and longwave radiation at the surface and TOA due to mineral dust particles at 12:00 UTC (AOD at 450 nm).
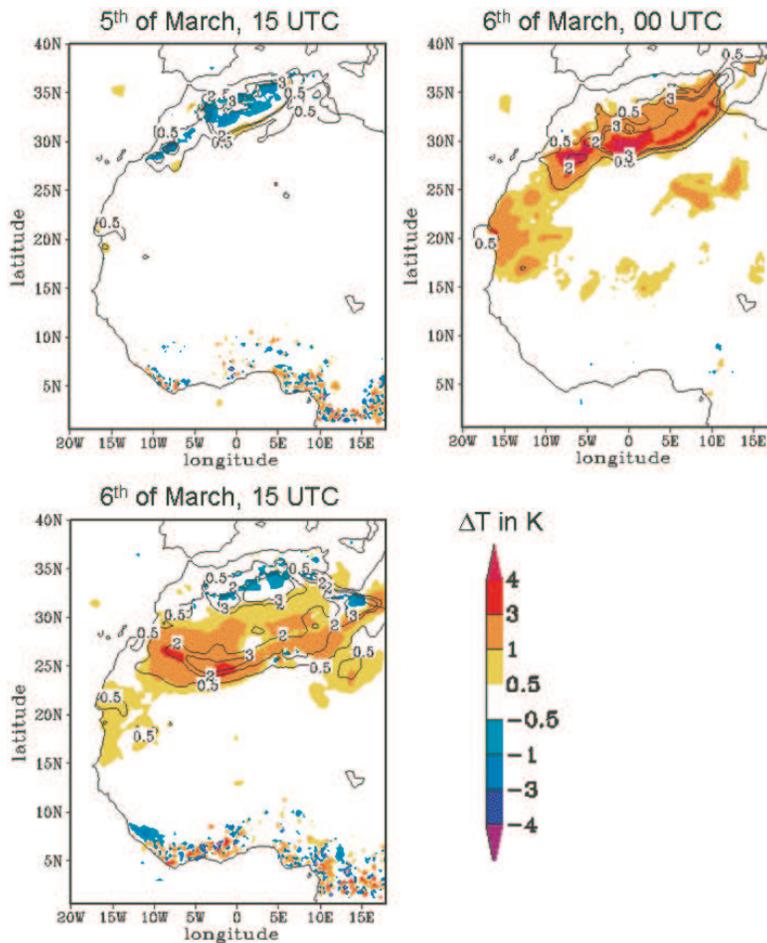
Fig. 8. Difference in 2 m temperature between runs F and CTRL and simulated AOD at 450 nm of run F (isolines) during the dust outbreak in March 2006.

Title Page

Abstract | Introduction

Conclusions | References

Tables | Figures

◀ | ▶|

◀ | ▶

Back | Close

Full Screen / Esc

Printer-friendly Version

Interactive Discussion

Printer-friendly Version

Interactive Discussion
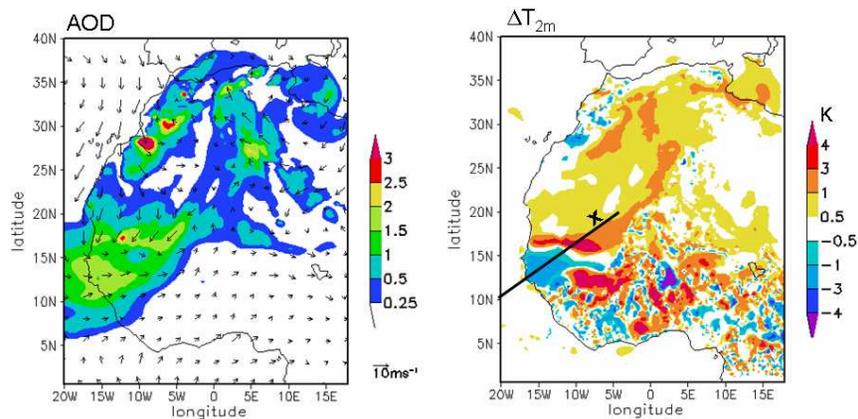
Fig. 9. Simulated AOD at 450 nm and 10 m wind vectors of run F (left) and difference in 2 m temperature in K between runs F and CTRL (right) on 21 June 2007, 15:00 UTC.
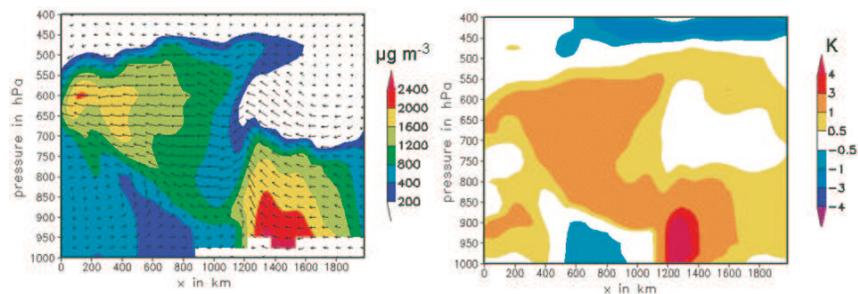
Fig. 10. Vertical cross section of mass concentration of mineral dust (left) and difference in potential temperature (right) along the line indicated by x in Fig. 9 on 21 June 2007, 15:00 UTC.